Superconductor
Science and
Technology

PAPER • **OPEN ACCESS**

Manufacturing and testing of robotic-wound segmented non-planar REBCO coil for distributed windings in superconducting rotating machines

To cite this article: Jianghong Wan *et al* 2026 *Supercond. Sci. Technol.* **39** 085001

Superconductor Science and Technology

OPEN ACCESS

RECEIVED
29 April 2026

REVISED
2 July 2026

ACCEPTED FOR PUBLICATION
21 July 2026

PUBLISHED
3 August 2026

PAPER

Manufacturing and testing of robotic-wound segmented non-planar REBCO coil for distributed windings in superconducting rotating machines

Jianghong Wan*, Mathias Noe, Magnus Dam, Tabea Arndt, David Irmle, Lukas Pfreundschuh and Francesco Grilli

Institute for Technical Physics, Karlsruhe Institute of Technology, DE-76344 Eggenstein-Leopoldshafen, Germany

* Author to whom any correspondence should be addressed.

E-mail: Jianghong.wan@kit.edu

Keywords: non-planar coil, superconducting rotating machine, distributed winding, segmentation method, robotic winding, no-insulation coil, REBCO

Abstract

Distributed windings offer significant electromagnetic advantages for fully superconducting rotating machines, especially higher power density. Non-planar REBCO coils are required for the realization of it but remain challenging to design and fabricate due to the limited strain tolerance of the REBCO layer. In this work, we extend a previously proposed single-turn segmented non-planar coil design to a 20-turn configuration, deriving the geometric parameters of each turn analytically to account for the finite tape thickness. Based on the parameterized coil geometry, we develop a robotic winding procedure using a discrete representation of the tool trajectory and orientation to enable controlled and repeatable tape placement. We validate the approach by manufacturing a no-insulation REBCO test coil and characterizing its electromagnetic performance at 77 K. A critical current of 70 A is measured, in good agreement with the modified load-line estimate of 74.5 A, and the measured central magnetic flux density deviates by less than 1 % from the Biot–Savart calculation.

1. Introduction

Second generation (2G) high-temperature superconducting (HTS) rare-earth barium copper oxide (REBCO) coated conductors, owing to their high critical current density under significant magnetic fields and relatively high operating temperatures, are of interest for armature windings in fully superconducting rotating machines [1]. Among winding configurations, distributed winding is particularly attractive because of its higher slot utilization and increased current loading, leading to higher specific power density [2], as well as reduced torque ripple compared to concentrated winding. However, the geometric design and the fabrication of the non-planar REBCO coils required for distributed windings remain challenging due to the limited mechanical strain tolerance of the REBCO layer [3–5].

A segmentation method for designing such non-planar coil geometries was previously established by the authors in [6], enabling direct construction of strain-controlled coil shapes by selectively combining predefined geometric segments including easy-way bending, twisting, and helix. A single-turn non-planar coil geometry for double-layer distributed winding was proposed and an initial prototype was manually wound and tested at 77 K, providing a first experimental validation of this approach. However, extending this work toward practical application requires both a multi-turn coil configuration and a manufacturing process capable of precise and repeatable tape placement.

Extending the single-turn non-planar coil design to a multi-turn configuration introduces additional geometric complexity. Each turn must preserve the segment layout of the reference turn while maintaining sufficient inter-turn spacing to accommodate the finite tape thickness. For non-planar coils, the spacing is not uniform but varies along the trajectory as the local tape orientation changes. Consequently, the geometric parameters of each turn cannot be obtained by a simple uniform offset, but must be determined individually through analytical formulation of each segment.

Manufacturing non-planar coils with REBCO tapes remains challenging, as the tape must be accurately placed on the coil frame [7] while maintaining constant tension [8] and avoiding excessive strain during the winding process [9]. Winding complex non-planar coil geometries requires coordinated control of both the tape's position and rotation angle throughout all winding operations [9]. Robotic winding technology provides a promising approach, enabling precise control of the winding tool motion to ensure accurate REBCO tape placement with constant tension and reduced risk of strain-induced damage [10]. The capability of this approach has been demonstrated at KIT through the successful winding of a superellipse-shaped HTS coil with hard-way bending. The segmentation method to coil design is particularly well-suited to this manufacturing approach. With this method, the parameterized description of each segment allows the winding tool trajectory and orientation to be derived directly, while the finite set of predefined segment types reduces the winding process to a sequence of modular and repeatable motion primitives.

This paper presents the design, robotic manufacturing, and electromagnetic characterization of a 20-turn robotic-wound segmented non-planar REBCO coil for double-layer distributed windings. The primary focus of this study is to validate the proposed coil geometry and the winding process. To simplify fabrication, a no-insulation configuration is adopted for the prototype, since turn-to-turn insulation is not critical at this stage of development. The multi-turn coil geometry design is described in section 2. Section 3 details the robotic winding process and coil assembly. Section 4 presents the critical current and central magnetic field measurements and compare them with simulation results.

2. Coil geometry design

This section presents the multi-turn coil geometry derived from the previously reported segmentation method [6]. The innermost turn is defined as the reference, and the remaining 19 turns are generated analytically to ensure geometric consistency across the full 20-turn configuration.

2.1. Design of the reference turn

The reference turn follows the same segment layout as the single-turn design reported in [6], comprising easy-way bending, twisting, and helix segments as shown in figure 1. Each segment is described analytically by its geometric parameters, which are summarized in table 1. Based on these parameters, the complete three-dimensional trajectory and orientation of the conductor can be fully determined.

The mechanical strain at the REBCO layer is evaluated at half the substrate thickness from the neutral plane using analytical formulations based on the segment geometry [11–13]. The irreversible compressive and tensile strain limits for REBCO tapes are approximately $\epsilon_{\mathrm{irr,com}} = -0.8\%$ and $\epsilon_{\mathrm{irr,ten}} = 0.5\%$, respectively [14]. Since the REBCO layer faces the former during the winding process, it is subjected to compressive strain after easy-way bending. To provide margin for additional strain contributions induced by winding, thermal effects, and Lorentz forces, a conservative design limit of 0.3 % is imposed on the intrinsic strain of each segment as shown in table 2.

2.2. 20-turn coil configuration

The 20-turn coil is constructed by extending each segment of the reference turn using analytical formulations that account for the finite thickness of the REBCO tape. The innermost turn serves as the geometric reference, and each subsequent turn is generated by applying a systematic offset relative to this reference.

For the easy-way bending segments, the bending radius and angle of the k-th turn are expressed as

$$r_k = r_0 + (k-1)\, d_{\mathrm{tot}}, \tag{1}$$

$$\theta_k = \theta_0 - \alpha_k, \tag{2}$$

where $k = 1, 2, \ldots, 20$ is the turn index and α_k represents the angular correction induced by the accumulated tape thickness in the twisting segments.

As illustrated in figure 1, due to the finite tape thickness, the centerline distance of adjacent turns differs between the beginning and the end of the twisting segments. This variation leads to a deviation in the tangent directions among different turns. To ensure tangent continuity between the bending and

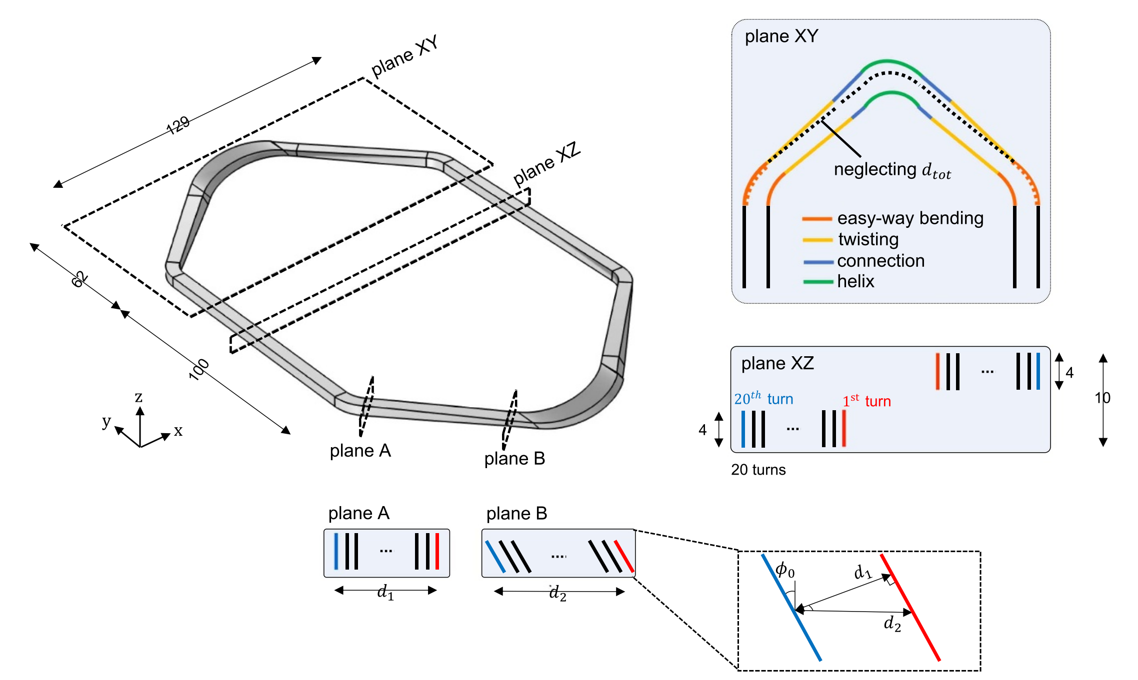

Figure 1. Geometry and dimensions of the non-planar coil for double-layer distributed winding. The coil consists of 20 turns wound from REBCO tape (4 mm in width and (0.155 mm in thickness) without turn-to-turn insulation. All dimensions are expressed in millimeters.

Table 1. Design parameters of each segment in the innermost turn.

Symbol	Description	Value	Unit
r_0	easy-way bending radius	10	mm
θ_0	easy-way bending angle	45	deg
$L_{\mathrm{tw},0}$	twisting length	50	mm
ϕ_0	twisting angle	30	deg
$L_{\mathrm{con},0}$	connection length	4	mm
R_0	helix radius	20.42	mm
p_0	helix pitch	64.16	mm
$t \in [t_s, t_e]$	helix range	$[0.66, 2.48]$	rad

Table 2. The minimum and maximum strain values of the innermost turn.

Symbol	Description	Value
$\epsilon_{\mathrm{n,min}}$	minimum easy-way bending strain	0
$\epsilon_{\mathrm{n,max}}$	maximum easy-way bending strain	−0.25%
$\epsilon_{\mathrm{t,min}}$	minimum twisting strain	0
$\epsilon_{\mathrm{t,max}}$	maximum twisting strain	0.015%
$\epsilon_{\mathrm{h,ax}}$	helix axial strain	−0.098%
$\epsilon_{\mathrm{h,trans}}$	helix transverse strain	0.024%
$\epsilon_{\mathrm{irr,com}}$	compressive strain limit	−0.8%
$\epsilon_{\mathrm{irr,ten}}$	tensile strain limit	0.5%

twisting segments, the bending angle must therefore be corrected by α_k, which is given by

$$\alpha_k = \arctan\left(\frac{d_{2,k} - d_{1,k}}{L_{\mathrm{tw0}}}\right), \tag{3}$$

$$d_{1,k} = (k-1)\, d_{\mathrm{tot}}, \tag{4}$$

$$d_{2,k} = \frac{d_{1,k}}{\cos(\phi_0)}, \tag{5}$$

Table 3. Specification of superpower SCS4050-AP (2012).

Symbol	Description	Value	Unit
w	tape width	4	mm
d_{sub}	substrate thickness	50	μm
d_{tot}	tape thickness	155	μm
d_{cu}	copper thickness	2×50	μm
I_c(s.f., 77 K)	I_c at self field, 77 K	128	A

where $d_{1,k}$ and $d_{2,k}$ denote the centerline offsets of the k-th turn relative to the reference (innermost) turn at the beginning and the end of the twisting segment, respectively, as illustrated in planes A and B in figure 1.

For the twisting segments, the twisting angle and length of the k-th turn are expressed as

$$\phi_k = \phi_0, \tag{6}$$

$$L_{\mathrm{tw},k} = \sqrt{L_{\mathrm{tw},0}^2 + (d_{2,k} - d_{1,k})^2}. \tag{7}$$

The analytical expressions above allow the geometric correction introduced by the finite tape thickness to be evaluated for each turn. For the outermost turn ($k = 20$) in our case, the angular correction to the bending angle reaches its maximum value of $\alpha_{20} \approx 0.52°$, corresponding to 1.16 % of the reference bending angle $\theta_0 = 45°$. Similarly, the twisting length of the outermost turn increases slightly to $L_{\mathrm{tw},20} \approx 50.002$ mm, representing a deviation of less than 0.005 % relative to the reference value. These results indicate that the geometric corrections induced by the tape thickness remain negligible for 20-turn coil configuration. Therefore, although the helix parameters should in principle be recalculated from the adjacent bending and twisting segments to ensure geometric continuity, the helix parameters of the reference turn are adopted for all subsequent turns in this design.

Based on the above analytical formulations, the complete multi-turn coil geometry can be derived from the reference turn. The specifications of the REBCO tape used in this study are listed in table 3, and the resulting coil geometry and dimensions are shown in figure 1.

3. Manufacturing of the test coil

To demonstrate the feasibility of manufacturing the proposed non-planar coil in a controlled and repeatable procedure, the Superpower REBCO tape was wound onto a dedicated 3D-printed coil support structure using the KIT robotic winding cell, and subsequently prepared for operation and testing in liquid nitrogen.

3.1. Robotic winding

In this study, robotic winding technology is applied to wind the proposed segmented non-planar coil, with the underlying hardware system described in detail in [10].

3.1.1. Winding tool trajectory

Since the proposed coil geometry consists of multiple segments without a unique global parametric curve, the winding tool trajectory is defined as a list of discrete coordinate points:

$$\{\boldsymbol{\beta}_i\}_{i=1}^{N}, \tag{8}$$

obtained by offsetting the sampled coil centerline $\boldsymbol{\gamma}_i$ along the tanget direction:

$$\boldsymbol{\beta}_i = \boldsymbol{\gamma}_i + \ell \boldsymbol{T}_i, \tag{9}$$

with $\boldsymbol{\gamma}_i$ denoting the coordinate point along the conductor centerline, $\boldsymbol{T}_i$ the corresponding unit tangent vector, ℓ the offset distance between the winding tool and the conductor, and N the number of discrete points.

3.1.2. Tool orientation

The orientation of the winding tool at $\boldsymbol{\beta}_i$ is defined such that its local coordinate system aligns with the Darboux frame of the coil at $\boldsymbol{\gamma}_i$ [15], as follws:

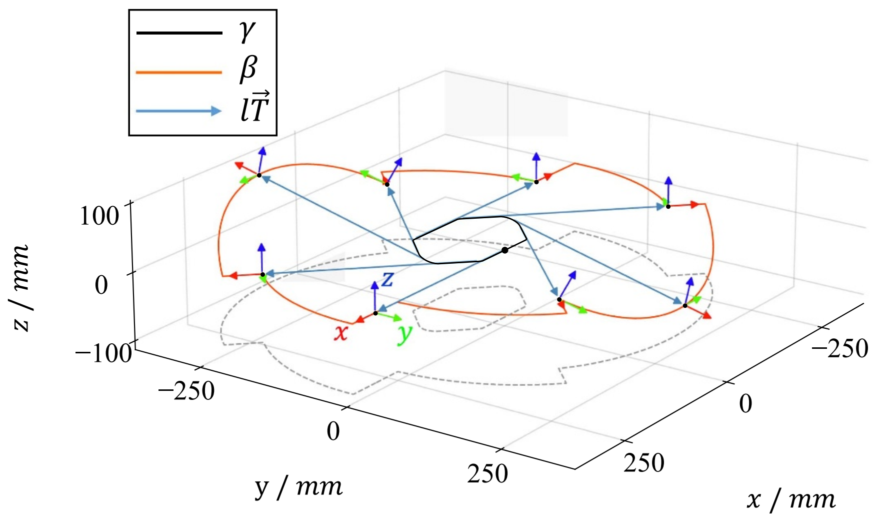

Figure 2. The non-planar coil centerline trajectory γ and the resulting winding tool trajectory β used for robotic winding. β is obtained by offsetting γ along the tangent direction $\boldsymbol{T}$ by a distance ℓ. At each point along the trajectory β, a local coordinate frame defined by the tangent $\boldsymbol{T}$, normal $\boldsymbol{N}$, and binormal $\boldsymbol{T}$ vectors describes the required orientation of the winding tool. The winding starts at the origin of the global coordinate system, where the initial TNB frame is aligned with the xyz axes. The projection of β onto the xy plane is also shown, illustrating the rotational motion of the workpiece positioner about the z-axis that is synchronized with the robot motion during the winding process.

Let $\{\mathbf{e}_x, \mathbf{e}_y, \mathbf{e}_z\}$ denote the initial orthonormal basis of the winding tool, which is aligned with the local frame of the coil as shown in figure 2 at the starting point (black marker). At each discrete point β_i, the target orientation is given by the local Darboux frame $\{\mathbf{T}_i, \mathbf{N}_i, \mathbf{B}_i\}$ at γ_i.

A rotation matrix $\mathbf{R}_i \in SO(3)$ is constructed such that

$$\boldsymbol{R}_i \begin{bmatrix} \boldsymbol{e}_x & \boldsymbol{e}_y & \boldsymbol{e}_z \end{bmatrix} = \begin{bmatrix} \boldsymbol{T}_i & \boldsymbol{N}_i & \boldsymbol{B}_i \end{bmatrix}. \tag{10}$$

Since $\{\boldsymbol{e}_x, \boldsymbol{e}_y, \boldsymbol{e}_z\}$ is the canonical basis, the rotation matrix can be directly written as

$$\boldsymbol{R}_i = \begin{bmatrix} \boldsymbol{T}_i & \boldsymbol{N}_i & \boldsymbol{B}_i \end{bmatrix}. \tag{11}$$

The rotation matrix is then decomposed into Z-Y-X intrinsic rotation Euler angles $(\theta_{x,i}, \theta_{y,i}, \theta_{z,i})$, corresponding to successive rotations about the z-, y-, and x-axes

$$\boldsymbol{R}_i = \boldsymbol{R}_z(\theta_{z,i})\, \boldsymbol{R}_y(\theta_{y,i})\, \boldsymbol{R}_x(\theta_{x,i}), \tag{12}$$

where the individual rotation matrices are given by

$$\boldsymbol{R}_x(\theta_x) = \begin{bmatrix} 1 & 0 & 0 \\ 0 & \cos\theta_x & -\sin\theta_x \\ 0 & \sin\theta_x & \cos\theta_x \end{bmatrix}, \tag{13}$$

$$\boldsymbol{R}_y(\theta_y) = \begin{bmatrix} \cos\theta_y & 0 & \sin\theta_y \\ 0 & 1 & 0 \\ -\sin\theta_y & 0 & \cos\theta_y \end{bmatrix}, \tag{14}$$

$$\boldsymbol{R}_z(\theta_z) = \begin{bmatrix} \cos\theta_z & -\sin\theta_z & 0 \\ \sin\theta_z & \cos\theta_z & 0 \\ 0 & 0 & 1 \end{bmatrix}. \tag{15}$$

Multiplying these matrices yields the full rotation matrix:

$$\boldsymbol{R} = \begin{bmatrix} \cos\theta_z\cos\theta_y & \cos\theta_z\sin\theta_y\sin\theta_x - \sin\theta_z\cos\theta_x & \cos\theta_z\sin\theta_y\cos\theta_x + \sin\theta_z\sin\theta_x \\ \sin\theta_z\cos\theta_y & \sin\theta_z\sin\theta_y\sin\theta_x + \cos\theta_z\cos\theta_x & \sin\theta_z\sin\theta_y\cos\theta_x - \cos\theta_z\sin\theta_x \\ -\sin\theta_y & \cos\theta_y\sin\theta_x & \cos\theta_y\cos\theta_x \end{bmatrix}. \tag{16}$$

The Euler angles at i-th point are obtained from the elements of $\boldsymbol{R}_i$ as

$$\theta_{y,i} = \arcsin(-R_{31}), \tag{17}$$

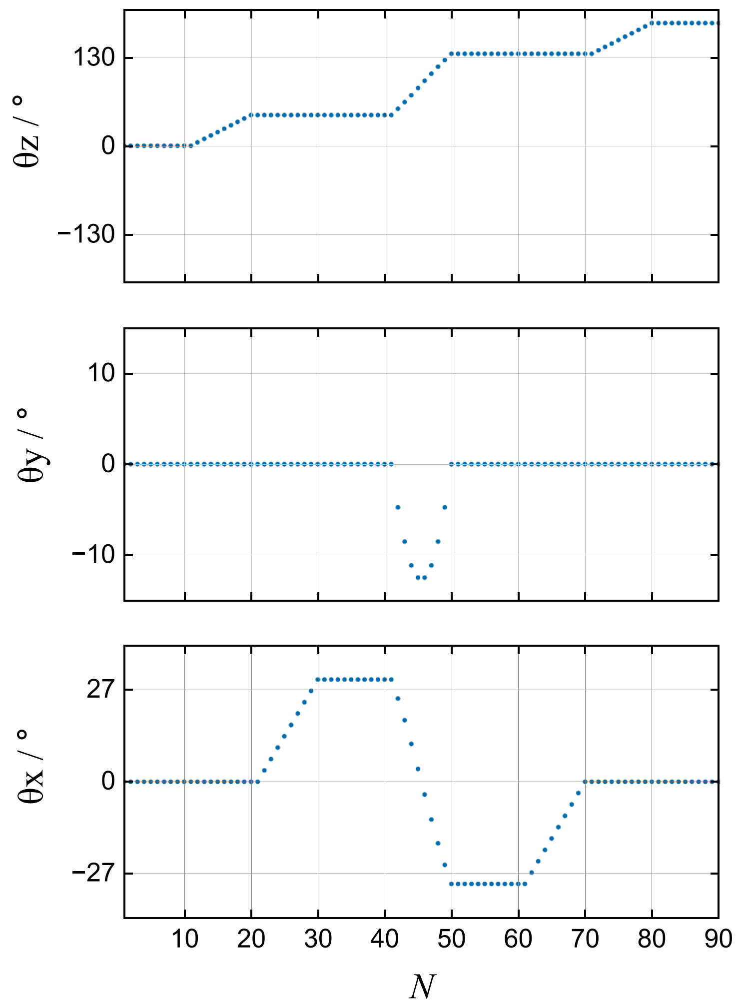

Figure 3. The winding tool rotation angles θ_z, θ_y, and θ_x as a function of the point index N.

$$\theta_{z,i} = \arctan 2\left(R_{21}, R_{11}\right), \tag{18}$$

$$\theta_{x,i} = \arctan 2\left(R_{32}, R_{33}\right), \tag{19}$$

where R_{ij} denotes the element of the rotation matrix in the i-th row and j-th column.

In the case of $\cos\theta_{y,i} \approx 0$, corresponding to a gimbal lock condition, the angles are evaluated using

$$\theta_{z,i} = \arctan 2\left(-R_{12}, R_{22}\right), \tag{20}$$

$$\theta_{x,i} = 0. \tag{21}$$

The resulting Euler angles along the winding trajectory are shown in figure 3 as a function of the discrete point index. Since the two coil ends are geometrically symmetric, only one coil end and the adjacent straight sections are shown for brevity.

3.1.3. Synchronous rotation of the workpiece positioner

To enable the fabrication of large-scale coils within the limited workspace of the robotic system as shown in figure 4, a synchronized rotation of the workpiece positioner is introduced.

The winding trajectory is predefined as a discrete set of points, and the tool orientation is specified at each point by the corresponding rotation angles. Both the trajectory points and the associated tool orientations are defined on the initial workpiece coordinate system W_0.

During execution, both the workpiece positioner and the coordinate system W_0 are rotated synchronously about the global z-axis. At the i-th step, the rotation angle is defined as

$$\psi_i = i \cdot \Delta\psi, \tag{22}$$

where $\Delta\psi = 2\pi/N$ is the angular increment, and N denotes the number of discrete trajectory points used to describe one turn of the coil.

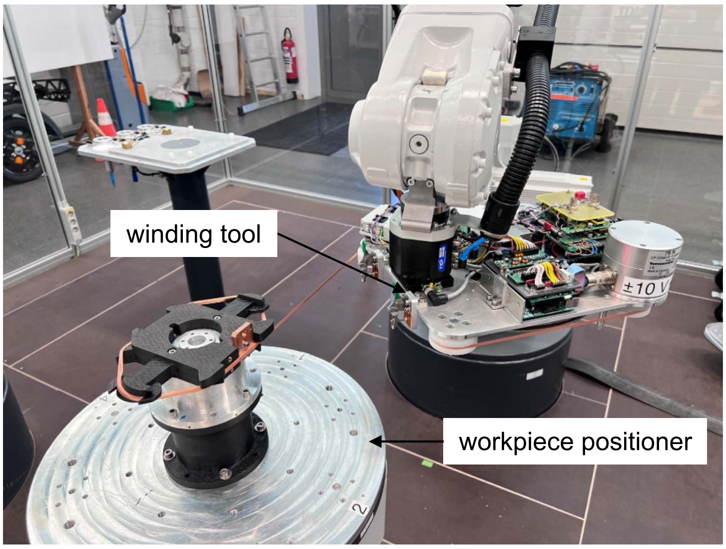

Figure 4. Robotic winding of the non-planar coil for distributed winding. The coil support structure is mounted on the workpiece positioner and rotates synchronously with it during the winding process.

The orientation of the workpiece coordinate system is then updated as

$$\boldsymbol{W}_i = \boldsymbol{R}_z(\psi_i)\,\boldsymbol{W}_0, \tag{23}$$

while the positioner rotates physically by the same angle in the same direction.

In this way, the predefined winding trajectory and tool orientations remain unchanged with respect to the rotating workpiece coordinate system, while the coil rotates in the global frame. This co-rotating approach preserves the relative relationship between the winding tool and the coil geometry and reduces the motion range required from the robot.

3.2. Coil construction

The trajectory and orientation of the winding tool, and the synchronous rotation of the workpiece positioner were programmed using RobotStudio. A dedicated coil assembly, including the coil support structure and the corresponding experimental setup, was designed and used in coil winding process.

3.2.1. Coil assembly design

The coil assembly is designed to support both the robotic winding process and the subsequent experimental characterization of the non-planar REBCO coil as shown in figure 5. The dedicated coil former is 3D-printed with the material of carbon fiber-reinforced nylon filament(Polymaker Fiberon PA6-CF20), providing geometric guidance for the predefined winding trajectory while ensuring sufficient mechanical stability during winding. The thermal contraction of this material upon cooling to 77 K is comparable to that of stainless steel, making it suitable for cryogenic applications. In this work, the coil former is retained during testing. However, the final coil could in principle be impregnated to maintain its shape and successively have its former removed, which is envisioned as a future step toward the machine integration.

Copper terminals are integrated into the assembly to serve as current leads in electromagnetic characterization experiments. The inner terminal is fixed to the coil holder and acts as the starting point of the winding, while the outer terminal is mounted after completion of the winding process. All contact surfaces are pre-tinned to facilitate reliable soldering between the REBCO tape and the electrical terminals.

3.2.2. Coil winding

The coil former is mounted on the turntable of the workpiece positioner, and the REBCO tape spool is installed on the robotic winding tool. The tape is oriented such that the superconducting layer faces the former during winding, ensuring compressive strain conditions in bending-dominated regions. The winding process is initiated by soldering the tape to the inner terminal, followed by the application of controlled tension of 20 N.

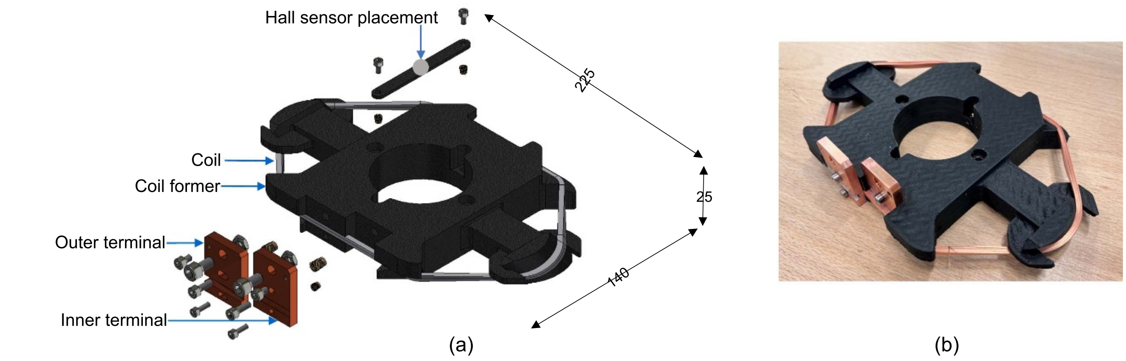

Figure 5. (a) Exploded view of the non-planar coil assembly for distributed winding. The 3D-printed support structure is made of carbon fiber reinforced nylon. The inner and outer terminals are made of copper, while the cap screws and nuts are made of stainless steel. All dimensions are expressed in millimeters. (b) The completed non-planar REBCO coil for distributed windings.

The coil is then wound without turn-to-turn insulation using the robotic winding strategy described in section 3.1, with synchronized motion between the robot and the positioner to ensure accurate placement of the tape along the prescribed trajectory. After completing the final turn, the tape is soldered to the outer terminal, forming a closed electrical circuit.

The completed non-planar multi-turn coil is shown in figure 5.

4. Experimental characterization and simulation validation

This section summarizes the experimental characterization and simulated validation of the robotic-wound segmented non-planar coil at 77 K. The measurement setup for critical current and magnetic field characterization is first described, followed by the experimental results. The critical current of the coil is then estimated using a load-line model that accounts for both the non-planar coil geometry and the angular and field dependence of the REBCO tape.

4.1. Measurements of magnetic field and critical current

The four-point method is used to measure the critical current of the coil [16]. Before the measurements, the total length of the REBCO tape in the coil is calculated. The corresponding voltage criterion is obtained by multiplying this length by the critical electric field $E_c = 1\,\mu\mathrm{V\,cm^{-1}}$.

4.1.1. Measurement setup

As shown in figure 6, four voltage taps are placed along the current path. Two taps are soldered directly onto the REBCO tape, denoted as $\mathrm{T_{in}}$ and $\mathrm{T_{out}}$, while two additional taps are attached to the copper terminals, denoted as $\mathrm{Cu_{in}}$ and $\mathrm{Cu_{out}}$. A Hall sensor positioned at the geometric center of the coil measures the magnetic field generated by the coil. Voltage signals from the taps and the Hall sensor output are recorded using a nanovoltmeter connected to a multiplexer that sequentially scans the measurement channels, while the operating current is monitored directly from the power supply.

For cryogenic testing, the coil assembly is mounted on a support plate with extended handles to allow safe immersion and removal from the cryogenic bath. The support plate is placed inside a thermally insulated container, which is gradually filled with liquid nitrogen until the entire coil and the lower part of the current leads are fully submerged.

4.1.2. Measurement procedure

The voltage across the superconducting coil is defined as

$$V_{\mathrm{coil}} = V_{\mathrm{T_{in}}} - V_{\mathrm{T_{out}}}, \tag{24}$$

which excludes the resistive voltage drop across the copper terminals. Additional voltages, $V_{\mathrm{Cu_{in}},\mathrm{Cu_{out}}}$, $V_{\mathrm{Cu_{in}},\mathrm{T_{in}}}$, and $V_{\mathrm{T_{out}},\mathrm{Cu_{out}}}$, are monitored to verify proper electrical contact throughout the measurement. Before ramping, the Hall sensor is calibrated at zero current to establish a stable baseline. The transport current is increased at a ramp rate of $1\ \mathrm{A\,s^{-1}}$ and paused every 5 A. Since the no-insulation coil can

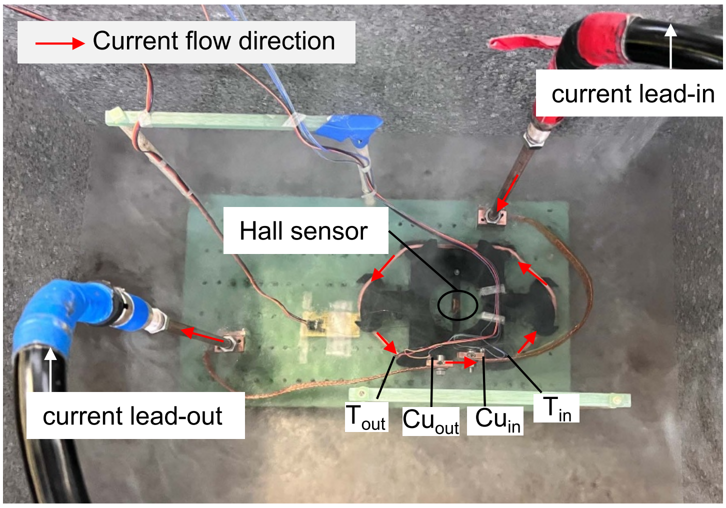

Figure 6. Setup for testing the coil in liquid nitrogen. Current is fed through current leads. The Hall sensor is placed at the coil center to measure the axial magnetic field. Four voltage taps are attached to measure the critical current and the terminal resistance.

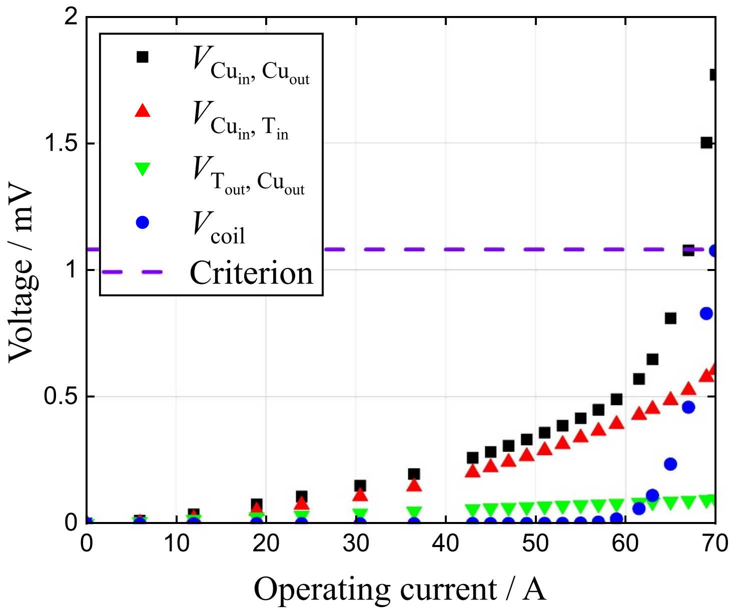

Figure 7. Measured *V-I* curves of the non-planar coil for distributed winding. $V_{Cu_{in},Cu_{out}}$ includes the voltage of the coil and both copper terminals, $V_{Cu_{in},T_{in}}$ indicates the voltage across the inner copper terminal, $V_{T_{out},Cu_{out}}$ indicates the voltage across the external copper terminal, and V_{coil} represents the voltage across the coil only.

exhibit transient voltage behavior associated with current redistribution during ramping, each pause is held until the voltage signals achieving a steady state. Near the critical voltage criterion, the ramp rate is reduced to 0.1 $\mathrm{A\,s^{-1}}$ with pauses every 2 A to protect the coil from possible damage and improve measurement resolution. The critical current $I_{c,mea}$ is determined using the 1 $\mu\mathrm{V\,cm^{-1}}$ electric field criterion, and the entire procedure is repeated twice to verify repeatability.

4.1.3. Measurement results

The measured steady-state voltages versus the operating current are shown in figure 7. The critical current of the coil is found to be $I_{c,mea} = 70$ A, at which V_{coil} reaches the voltage criterion. Linear interpolation between adjacent data points is applied to accurately determine the corresponding current value. The central magnetic flux density as a function of the operating current is presented in figure 8.

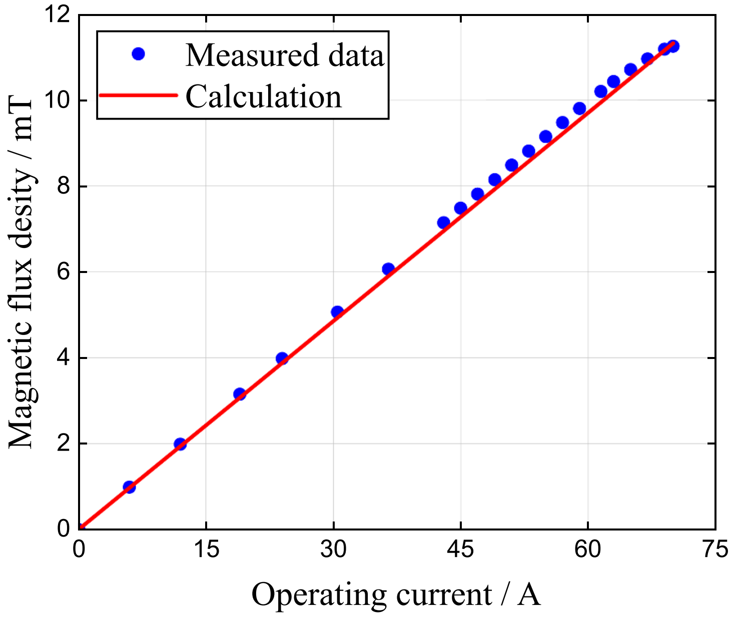

Figure 8. Measured central magnetic flux density and the values calculated from the coil geometry and the operating current using the Biot-Savart law.

4.2. Simulation

The critical current of the coil is estimated using the load-line method based on two critical current I_c criteria, which are [17]:

(i) MAX criteria, I_c is the current at which the voltage drop per unit length reaches the critical electric field E_c in at least one conductor.

(ii) AVG criteria, I_c is the current at which the average voltage drop per unit length reaches E_c.

The load-line method has been widely applied in the analysis of superconducting devices [18–20]. In this approach, the magnetic field inside one conductor is calculated at each operating current under the assumption of uniform current density distribution. Based on the $I_c(B,\theta)$ characteristic of a short tape sample, the corresponding critical current is determined. The calculation is repeated for increasing values of operating current until the calculated critical current equals the operating current, at which point the maximum current-carrying capacity of the conductor is determined [21].

In this work, the load-line method is extended to account for the non-planar geometry of the coil. At each operating current, the magnetic field distribution of the coil is computed using a 3D finite element (FE) model, as shown in figure 10. With the MAX criterion, the critical current is estimated by monitoring the magnetic field distribution along the innermost turn, which experiences the highest local field. The critical current distribution along the innermost turn is evaluated with the experimentally measured $I_c(B,\theta)$ characteristics of a short tape sample obtained in this work, as shown in figure 10. Here $\theta = 90^\circ$ is defined as the field parallel to the tape's wider surface. The minimum value of this distribution is then extracted and recorded as a function of operating current. The intersection of the resulting minimum critical current curve with the operating current line gives the estimated coil critical current of, $I_{c,LL} = 71.8$ A, as shown in figure 11. The corresponding minimum critical current location is identified as point P1 in figure 9, which is located in the winding head region.

With the AVG criterion, the critical current is estimated using the modified load-line method, following [21]. The critical current distribution along the entire coil, including 20 turns, is calculated at each operating current as aforementioned. instead of finding the crossing point between the operation currents and the minimum critical currents along the innermost turn, the average electric field of the coil is calculated according to the $E - J$ relation as follow,

$$\rho_{\mathrm{HTS}} = \frac{E_c}{J_c(B,\theta)} \left(\frac{J}{J_c(B,\theta)} \right)^{n-1}, \tag{25}$$

$$E = \rho_{\mathrm{HTS}} J, \tag{26}$$

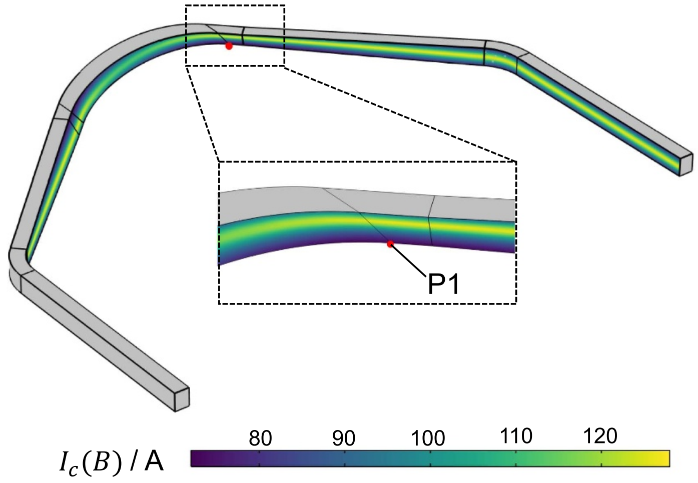

Figure 9. 3D FE electromagnetic model in COMSOL. Only half of the coil geometry is considered due to the symmetry. P1 is the location on the innermost turn where the minimum critical current occurs.

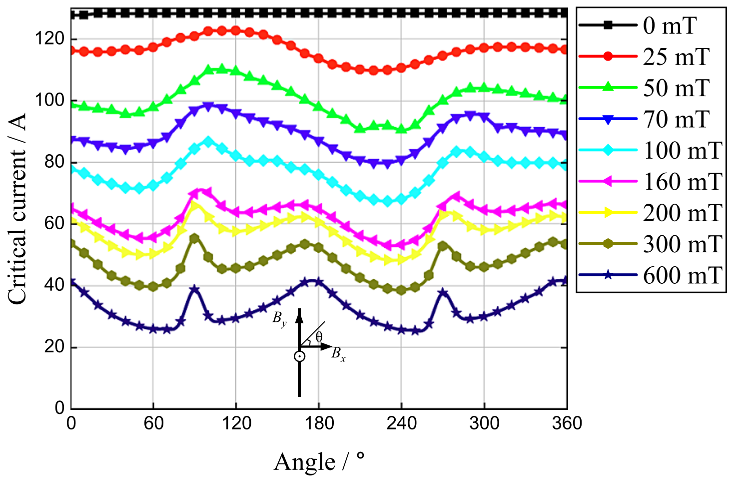

Figure 10. Critical current of the HTS tape SCS4050-AP as a function of orientation and amplitude of an applied field in liquid nitrogen at 77 K, measured in this work.

where J is the current density at the given operating current, obtained under the same uniform current density assumption as above.

The calculation is repeated for increasing values of operating current until the average electric field per unit length of the coil reaches E_c, which gives the estimated coil critical current of $I_{c,\text{modified LL}} = 74.5$ A.

4.3. Discussion

The comparison between experimental and simulated results is presented in table 4.

For magnetic flux density, the measured values show good agreement with the Biot-Savart calculation over the entire current range as shown in figure 8, with a deviation of less than 1% at $I_{c,\text{mea}} = 70$ A, where the measured and calculated values are 11.3 mT and 11.3 mT, respectively. The linear dependence of the central field on the operating current is well reproduced by the calculation, indicating that the manufactured coil geometry is consistent with the design.

For critical current, compared with the measured result $I_{c,\text{mea}} = 70$ A, the deviation of $I_{c,\text{LL}}$ is 2.6%, whereas the deviation of $I_{c,\text{modified LL}}$ increases to 6.4%. The estimate of $I_{c,\text{LL}}$ is based on the worst-point criterion, which provides a conservative estimate of the coil's current-carrying capacity with a safety margin. By contrast, $I_{c,\text{modified LL}}$ is evaluated with the average criterion, thereby enabling a more direct comparison with $I_{c,\text{mea}}$. The deviation $\delta_{I_{c,\text{modified LL}}}$ may be attributed to the assumption of uniform current density distribution, length uniformity of $I_c(B,\theta)$ characteristics, and manufacturing tolerances that are

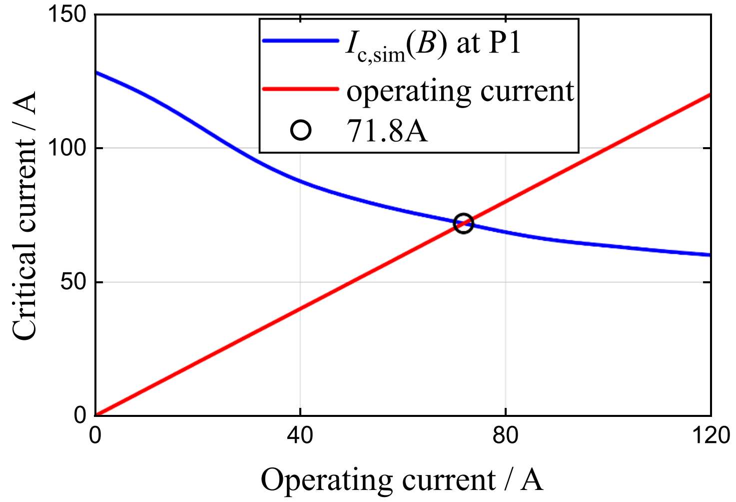

Figure 11. Load-line method for the non-planar coil from 3D finite element simulation. The $I_{c,sim}(B)$ line of P1 crosses the operating current line at 71.8 A.

Table 4. Comparison between measurement and simulation.

Symbol	Description	Value	Unit
$I_{c,mea}$	measured coil critical current	70	A
$I_{c,LL}$	simulated critical current (load-line method)	71.8	A
$I_{c,modified\ LL}$	simulated critical current (modified load-line method)	74.5	A
$\delta_{I_{c,LL}}$	deviation of $I_{c,LL}$ from $I_{c,mea}$	2.6%	—
$\delta_{I_{c,modified\ LL}}$	deviation of $I_{c,modified\ LL}$ from $I_{c,mea}$	6.4%	—
$B_{0,mea}$	measured central magnetic flux density at $I_{c,mea}$	11.3	mT
$B_{0,cal}$	calculated central magnetic flux density $I_{c,mea}$	11.3	mT
δ_{B_0}	deviation of $B_{0,cal}$ from $B_{0,mea}$	0.0%	—

not considered in the present models. However, $\delta_{I_{c,modified\ LL}} = 6.4\%$ is still considered acceptable, indicating that the proposed non-planar coil can be reliably manufactured using robotic winding technology without significant degradation of the critical current.

5. Conclusion

We demonstrate the feasibility of the proposed non-planar REBCO coils for double-layer distributed windings in superconducting rotating machines through coil design, robotic winding, and electromagnetic characterization of a 20-turn test coil. We build the multi-turn coil geometry based on the previously proposed single-turn coil geometry designed with the segmentation method. Based on the parameterized coil geometry, we develop a robotic winding strategy with discrete winding tool trajectory points and corresponding tool orientations. The 20-turn test coil without turn-to-turn insulation is successfully fabricated using the KIT robotic winding cell and tested in liquid nitrogen at 77 K, and the experimental results are compared with simulation. The agreements confirm that the proposed multi-turn non-planar coil geometry, designed using the segmentation method, can be reliably manufactured using the robotic winding system without causing a significant degradation in the critical current.

Future work will focus on characterizing the proposed coil under conditions more relevant to rotating machine applications, including AC loss measurements on an insulated coil. In parallel, the coil structure will be further optimized for machine integration, for example by removing the coil former to allow the coils to be overlapped as required in double-layer distributed winding configurations.

Acknowledgments

The authors thank the staff at the Energy Laboratory and the Magnet Laboratory in ITEP at KIT for their invaluable support in coil construction and cryogenic testing. We are particularly grateful to Frank

Gretschmann and Johann Willms for coil soldering; Matthias Eisele and Marion Kläser for technical advice; Quoc Hung Pham for assistance with experiments; Sonja Schlachter and Rainer Gehring for experimental setup support; and Uwe Walschburger for mechanical work.

Data availability statement

All data that support the findings of this study are included within the article (and any supplementary files).

Appendix. List of symbols

The symbols used in this paper are summarized in tables A1–A3, organized according to their respective contexts: coil geometry design, robotic winding procedure, and electromagnetic characterization.

Table A1. Symbols related to geometry.

Symbol	Description	Unit
k	turn index	—
r_0	easy-way bending radius of the reference turn	mm
r_k	easy-way bending radius of the k-th turn	mm
θ_0	easy-way bending angle of the reference turn	deg
θ_k	easy-way bending angle of the k-th turn	deg
α_k	angular correction for the k-th turn	deg
$L_{\mathrm{tw},0}$	twisting length of the reference turn	mm
$L_{\mathrm{tw},k}$	twisting length of the k-th turn	mm
ϕ_0	twisting angle of the reference turn	deg
ϕ_k	twisting angle of the k-th turn	deg
$L_{\mathrm{con},0}$	connection length of the reference turn	mm
R_0	helix radius of the reference turn	mm
p_0	helix pitch of the reference turn	mm
t_0	helix parameter of the reference turn	rad
t_{s}	start value of the helix parameter range	rad
t_{e}	end value of the helix parameter range	rad
$d_{1,\mathrm{k}}$	centerline offset at the beginning of the twisting segment for the k-th turn	mm
$d_{2,\mathrm{k}}$	centerline offset at the end of the twisting segment for the k-th turn	mm
w	tape width	mm
d_{tot}	total tape thickness	μm
d_{sub}	substrate thickness	μm
d_{cu}	copper stabilizer thickness	μm
$\epsilon_{\mathrm{n,min}}$	minimum strain in easy-way bending segment	—
$\epsilon_{\mathrm{n,max}}$	maximum strain in easy-way bending segment	—
$\epsilon_{\mathrm{t,min}}$	minimum strain in twisting segment	—
$\epsilon_{\mathrm{t,max}}$	maximum strain in twisting segment	—
$\epsilon_{\mathrm{h,ax}}$	axial strain in helix segment	—
$\epsilon_{\mathrm{h,trans}}$	transverse strain in helix segment	—
$\epsilon_{\mathrm{irr,com}}$	irreversible compressive strain limit of REBCO tape	—
$\epsilon_{\mathrm{irr,ten}}$	irreversible tensile strain limit of REBCO tape	—

Table A2. Symbols related to winding procedure.

Symbol	Description	Unit
γ	coil centerline trajectory	mm
γ_i	i-th discrete point on the coil centerline	mm
β	winding tool trajectory	mm
β_i	i-th discrete point on the winding tool trajectory	mm
ℓ	offset distance between winding tool and conductor	mm
T	unit tangent vector of the coil centerline	—
N	unit normal vector of the coil centerline	—
B	unit binormal vector of the coil centerline	—
$\mathrm{e}_x, \mathrm{e}_y, \mathrm{e}_z$	initial orthonormal basis of the winding tool	—
R_i	rotation matrix of the winding tool at point i	—
$\mathrm{R}_x, \mathrm{R}_y, \mathrm{R}_z$	elemental rotation matrices about the x-, y-, and z-axes	—
$\theta_{x,i}$	Euler rotation angle about the local x-axis at point i	deg
$\theta_{y,i}$	Euler rotation angle about the local y-axis at point i	deg
$\theta_{z,i}$	Euler rotation angle about the local z-axis at point i	deg
ψ_i	rotation angle of the workpiece positioner at step i	rad
$\Delta\psi$	angular increment of the workpiece positioner	rad
W_0	initial workpiece coordinate system orientation	—
W_i	workpiece coordinate system orientation at step i	—
N	number of discrete trajectory points per turn	—
i	index of discrete trajectory points or rotation steps	—

Table A3. Symbols related to electromagnetic characterization.

Symbol	Description	Unit
I_{op}	operating current	A
I_{c}	critical current of tape at self-field and 77 K	A
$I_{\mathrm{c,mea}}$	measured critical current of the coil	A
$I_{\mathrm{c,LL}}$	coil critical current estimated by load-line method	A
$I_{\mathrm{c,modified\ LL}}$	coil critical current estimated by modified load-line method	A
B	magnetic flux density	T
B_0	central magnetic flux density of the coil	T
$B_{0,\mathrm{mea}}$	measured central magnetic flux density	T
$B_{0,\mathrm{cal}}$	calculated central magnetic flux density	T
θ	angle between magnetic field and tape wide surface normal	deg
E_c	critical electric field criterion	μV cm^{-1}
V_{coil}	voltage across the superconducting coil	V
$V_{\mathrm{T_{in}}}$	voltage at the inner tape voltage tap	V
$V_{\mathrm{T_{out}}}$	voltage at the outer tape voltage tap	V
$V_{\mathrm{Cu_{in},Cu_{out}}}$	voltage between the two copper terminals	V
$V_{\mathrm{Cu_{in},T_{in}}}$	voltage between inner copper terminal and inner tape tap	V
$V_{\mathrm{T_{out},Cu_{out}}}$	voltage between outer tape tap and outer copper terminal	V
$\delta_{I_{\mathrm{c,LL}}}$	deviation between measured and simulated critical current $I_{\mathrm{c,LL}}$	%
$\delta_{I_{\mathrm{c,modified\ LL}}}$	deviation between measured and simulated critical current $I_{\mathrm{c,modified\ LL}}$	%
$\delta_{\mathrm{B_0}}$	deviation between measured and calculated central magnetic flux density	%
P1	location of minimum critical current on the innermost turn	—

ORCID iDs

Jianghong Wan 0009-0002-6587-3315
Mathias Noe 0009-0006-5870-968X
Magnus Dam 0000-0002-6707-9548
Tabea Arndt 0000-0002-7797-8862
Francesco Grilli 0000-0003-0108-7235

References

[1] Chow C C, Ainslie M D and Chau K 2023 *Energy Rep.* **9** 1124–56
[2] Lipo T A 2017 *Introduction to AC Machine Design* (Wiley)
[3] Ilin K, Yagotintsev K, Zhou C, Gao P, Kosse J, Otten S, Wessel W, Haugan T, Van Der Laan D and Nijhuis A 2015 *Supercond. Sci. Technol.* **28** 055006

[4] Markiewicz W and Swenson C 2010 *Supercond. Sci. Technol.* **23** 045017
[5] Polikarpova M, Lukyanov P, Abdyukhanov I, Pantsyrny V, Vorobyeva A, Khlebova N, Sudyev S, Shikov A and Guryev V 2013 *IEEE Trans. Appl. Supercond.* **24** 6600604
[6] Wan J, Noe M, Dam M and Arndt T 2026 *IEEE Trans. Appl. Supercond.* **36** 5201609
[7] Huslage P, Schuler T, Gil P F, Brack V, Schmeling D, Orona D A R, von Schoenberg E, Thun T, Smoniewski J and Stenson E V 2026 *IEEE Trans. Appl. Supercond.* **36** 4201405
[8] Schmeling D, Russo M, Gebreamlak B, Kiker T, Skrypek A, Hightower A, Xue J, Chen S, Sohaib S and Martinez C 2025 arXiv:2510.07042
[9] Yang S, Song W, Park J, Kim G, Huang J Y, Hahn S, Choi S, Kang H and Hahn G 2024 *IEEE Trans. Appl. Supercond.* **34** 4801304
[10] Dam M and Arndt T 2025 *Supercond. Sci. Technol.* **38** 125004
[11] van der Laan D C and Ekin J 2008 *Supercond. Sci. Technol.* **21** 115002
[12] Wang X, Arbelaez D, Caspi S, Prestemon S O, Sabbi G and Shen T 2017 *IEEE Trans. Appl. Supercond.* **27** 6604010
[13] Takayasu M, Chiesa L, Bromberg L and Minervini J V 2012 *Supercond. Sci. Technol.* **25** 014011
[14] Otten S, Kario A, Kling A and Goldacker W 2016 *Supercond. Sci. Technol.* **29** 125003
[15] Connolly C 2009 *Ind. Robot: Int. J.* **36** 540–5
[16] Yu D, Liu H, Zhang X and Gong T 2018 *Materials* **11** 339
[17] Zermeño V, Sirois F, Takayasu M, Vojenciak M, Kario A and Grilli F 2015 *Supercond. Sci. Technol.* **28** 085004
[18] Song X, Mijatovic N, Kellers J, Bührer C, Rebsdorf A V, Hansen J, Christensen M, Krause J, Wiezoreck J and Pütz H 2017 *IEEE Trans. Appl. Supercond.* **27** 5201105
[19] Goldacker W, Frank A, Kudymow A, Heller R, Kling A, Terzieva S and Schmidt C 2009 *Supercond. Sci. Technol.* **22** 034003
[20] Staines M, Glasson N, Pannu M, Thakur K P, Badcock R, Allpress N, D'Souza P and Talantsev E 2012 *Supercond. Sci. Technol.* **25** 014002
[21] Liu Y, Ou J, Grilli F, Schreiner F, Zermeno V M R, Zhang M and Noe M 2019 *Supercond. Sci. Technol.* **32** 014001